Weak-inertial effects on destabilized receding contact lines

Akhil Varma [*]

Max Planck Institute for the Physics of Complex Systems, *Nöthnitzer Str. 38, 01187 Dresden, Germany*

It is known that, beyond a critical speed, the straight contact line of a partially -wetting liquid destabilizes into a corner. One of the earliest theoretical works exploring this phenomenon [Limat and Stone, Europhys. Lett. **65**, 365 (2004)] elicited a self-similar conical structure of the interface in the viscous regime. However, noting that inertia is not expected to be negligible at contact line speeds close to and beyond the critical value for many common liquids, we provide the leading-order inertial correction to their solution. In particular, we find the self-similar corrections to the interface shape as well as the flow field, and also determine their scaling with the capillary number. We find that inertia invariably modifies the interface into a cusplike shape with an increased film thickness. Furthermore, when incorporating contact line dynamics into the model, resulting in a narrowing of the corner as the contact line speed increases, we still observe an overall increase in the inertial contribution with speed despite the increased confinement.

I. INTRODUCTION

There is something intriguing about raindrops sliding down a window pane that fascinates us all on a rainy day. A keen observer might notice the drops speeding up as they slide down under gravity, forming long tails or rivulets that eventually break into smaller drops. This is a classic example of contact line destabilization. The capillary number, which is the dimensionless velocity of the contact line formed by the liquid interface and the solid surface, is the key player in this phenomenon. It is defined as $Ca = \eta V/\gamma$, where η is the viscosity of the liquid, γ is its surface tension, and V is the velocity of the moving contact line. It is beyond a critical value Ca_{cr}, that a straight contact line destabilizes and starts to entrain air (at the advancing front) or form cornered tails (at the receding end). For many common liquids, the critical value at the receding contact line is $Ca_{cr} \sim O(10^{-3})$.

The instability of receding contact lines of partially wetting liquids was addressed as early as the works of Blake and Ruschak [1] and Petrov and Sedev [2]. They observed that beyond a critical capillary number, a straight receding contact line transforms into a wedge or corner having some semiopening angle ϕ. The slanted orientation of the contact line keeps its normal component of velocity below the threshold for wetting transition. Furthermore, they observed that exceeding the critical capillary number did not alter the normal velocity of the (destabilized) contact line. Instead, it consistently maintained the critical value by adjusting its opening angle accordingly [2]. This is given by the simple phenomenological relation, $\sin \phi \propto 1/Ca$.

---

[*]Contact author: varma@pks.mpg.de; akhil@varma.net

Since this work, many experimental and theoretical studies followed which aimed at understanding the instability [3–5] as well as the detailed shape of the destabilized contact line [6–8]. However, the mechanism of this instability is not yet fully understood and is still an active area of research [9,10]. A comprehensive understanding of the contact line dynamics is indispensable for many engineering applications ranging from precision thin-film coatings, immersion lithography, nanofabrication and inkjet printing [11,12] to the design of liquid-repellent and antifogging surfaces [13]. They are also crucial for microfluidics and lab-on-chip technologies [14].

For a drop of viscous liquid moving down an incline, the instability is observed to occur first at the receding (rear) end, giving rise to the classical "teardrop" appearance. At velocities much higher than this critical value, the sharp corner transforms into a cusp, eventually breaking into drops at even higher velocities through a pearling instability [3,6,15]. The flow close to the corner is viscous dominated and hence can be approximated as a Stokes flow. This realization led Limat and Stone [16], and later Snoeijer *et al.* [17] to determine the interface profile and the flow field near the receding contact line using the lubrication theory, assuming a slowly varying interface profile near the corner. The theory matches well with the flow field observed in experiments of sliding silicone oil drops [17]. However, for fast-moving contact lines, inertial effects can be significant [7,18]. For example, consider water and silicone oil (100 cP) drops having a critical capillary number $\mathrm{Ca_{cr}} \approx 4 \times 10^{-3}$ and mercury, having $\mathrm{Ca_{cr}} \approx 1.5 \times 10^{-3}$ [6,7]. The drop velocities in these experiments are typically $10 - 100$ cm s^{-1} for water and mercury and $0.1 - 1$ cm s^{-1} for silicone oil. For these velocities the Reynolds number, which compares the inertial with the viscous effects, at distances of $l = 10 - 100$ μm from the corner turns out to be $\mathrm{Re}_l \sim 0.01 - 0.1$ for silicone oil, $\sim 1 - 10$ for water and $\sim 10 - 100$ for mercury. The low Reynolds number for silicone oil probably explains why the model with Stokes flow approximation agrees well with experiments. However, the large Reynolds number in the case of water and mercury drops indicates that inertial effects are dominant, even amounting to orders of 10^3 at the scale of the drops [7]. Thus, it seems that inertia cannot be excluded in the models of moving contact lines of these liquids. Prior theoretical works in this area have largely focused on the role of inertia near straight contact lines [19–21] or fully wetted films [22,23], but studies on cornered contact lines are scarce. For dewetting corners, Kim *et al.* [24] suggested using an effective dynamic pressure in the classical lubrication theory to mimic inertia. However, this results in a solution that is qualitatively indifferent from the noninertial case. Here, we will use a regular perturbation approach to systematically determine the inertial contribution and establish the correct scaling associated with it.

In this theoretical work, we shall focus on determining the inertial effects solely on *receding* destabilized contact lines. The mechanism of the instability is in itself quite complex and is beyond the scope of this work. Thus, for our analysis, we shall presuppose that the contact line is destabilized and forms a corner on the solid surface, as observed in experiments. Our objective then is to determine the shape of the interface and flow field within. To this end, we closely follow the analyses of Limat and Stone [16] and Snoeijer *et al.* [17] and improve on their solution by introducing weak-inertial corrections in Sec. II. In Sec. III we solve the boundary value problem for the interface profile, which gives us the leading-order effect of inertia near the contact line. The self-similar form of the inertial correction is obtained here. Taking water and mercury as example liquids, the inertial corrections to their interface shape and the flow field are discussed in Sec. IV. Finally, a summary of our key findings and relevant discussions are offered in Sec. V.

II. PROBLEM FORMULATION

Consider the steady motion of the contact line of a partially wetting liquid over a solid surface (at $z = 0$ plane) with a velocity V. As an illustrative example, we take the case of a drop sliding along the x axis as shown in Fig. 1. Let the liquid have a density ρ and viscosity η. The shape of the liquid interface is described by its height from the solid surface, $h(x, y)$. Close to the receding contact line, we assume a gradual variation of the interface height. We also assume the characteristic height of the interface, a, to be much smaller than the other dimensions, which have a characteristic length
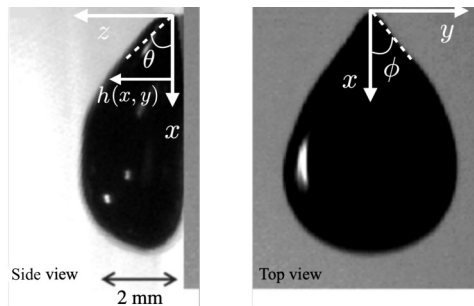
FIG. 1. Coordinate system used for the analysis of destabilized receding contact line. Shown here are the side and top view snapshots of a mercury drop sliding on a glass surface from the experiments of Puthenveettil *et al.* [7]. The liquid interface is at $z = h(x, y)$. The semiopening angle of the contact line and the local side angle of the interface are denoted by ϕ and θ, respectively. Dark grey is the solid surface (adapted with permission from [7].)

l. This allows for a separation of scales between the planar (x, y) and the normal (z) directions, which is done by introducing the small parameter, $a/l = \delta \ll 1$. We first rescale all the physical quantities with their respective characteristic values to obtain the corresponding dimensionless quantities (denoted by $\bar{\bullet}$). For example, the dimensionless coordinates $(\bar{x}, \bar{y}, \bar{z}) = (x/l, y/l, z/a)$, velocity field $(\bar{u}_x, \bar{u}_y, \bar{u}_z) = (u_x/V, u_y/V, u_z/(\delta V))$, and pressure field $\bar{p} = p\delta^2 l/(\eta V)$. Note that we have rescaled pressure using the lubrication pressure, rather than inertial, as we are interested in predominantly viscous flows.

A. Momentum conservation

The steady-state momentum conservation within the liquid is given by the Navier-Stokes equation, written in planar (x, y) and normal (z) directions, respectively, as

$$\delta^2 \bar{\Delta}\bar{\boldsymbol{u}} + \frac{\partial^2 \bar{\boldsymbol{u}}}{\partial \bar{z}^2} - \bar{\boldsymbol{\nabla}}\bar{p} = \delta^2 \mathrm{Re}_l \left(\bar{\boldsymbol{u}} \cdot \bar{\boldsymbol{\nabla}}\bar{\boldsymbol{u}} + \bar{u}_z \frac{\partial \bar{\boldsymbol{u}}}{\partial \bar{z}} \right), \tag{1}$$

$$\delta^2 \frac{\partial^2 \bar{u}_z}{\partial \bar{z}^2} - \frac{\partial \bar{p}}{\partial \bar{z}} = \delta^4 \mathrm{Re}_l \left(\bar{\boldsymbol{u}} \cdot \bar{\boldsymbol{\nabla}}\bar{u}_z + \bar{u}_z \frac{\partial \bar{u}_z}{\partial \bar{z}} \right). \tag{2}$$

Here, $\bar{\boldsymbol{u}} = (\bar{u}_x, \bar{u}_y)$, $\bar{\boldsymbol{\nabla}} = (\partial/\partial \bar{x}, \partial/\partial \bar{y})$ is the planar gradient, and $\bar{\Delta} = \partial^2/\partial \bar{x}^2 + \partial^2/\partial \bar{y}^2$ is the planar Laplacian. $\mathrm{Re}_l = lV\rho/\eta$ is the Reynolds number based on the larger length scale, l. Classical lubrication theory ignores the inertial term by assuming small values of $\mathrm{Re}_l \lesssim 1$. In contrast, here we consider the regime where $\mathrm{Re}_l \gg 1$, so as to retain the contribution of inertia. However, when the Reynolds number is sufficiently large, typically $\mathrm{Re}_l \gtrsim \delta^{-2}$, boundary layer separation starts coming into the picture [25]. To avoid this complication, we limit our analysis to the moderate inertial regime defined by $1 \ll \mathrm{Re}_l \ll \delta^{-2}$, i.e., $\mathrm{Re}_l \sim O(\delta^{-1})$. So now, by neglecting terms of $O(\delta^2)$ and smaller, (1) and (2) reduce to

$$\frac{\partial^2 \bar{\boldsymbol{u}}}{\partial \bar{z}^2} - \bar{\boldsymbol{\nabla}}\bar{p} = \epsilon \, (\bar{\boldsymbol{u}} \cdot \bar{\boldsymbol{\nabla}})\bar{\boldsymbol{u}} \quad \text{and} \tag{3}$$

$$\frac{\partial \bar{p}}{\partial \bar{z}} = 0 \tag{4}$$

where $\epsilon = \delta^2 \, \mathrm{Re}_l \sim O(\delta)$ is a small parameter. Comparison with full numerical simulations of channel flow has shown the "inertial thin-film equations" in (3) and (4) to be accurate even for much higher values of $\epsilon(\sim 1 - 10)$ [26]. To obtain the velocity field $\bar{\boldsymbol{u}}$, one has to integrate the expression (3) between $\bar{z} = 0$ and $\bar{z} = \bar{h}(\bar{x}, \bar{y})$, with the following boundary conditions in the

laboratory frame-of-reference: (i) no-slip at the solid surface, $\bar{\boldsymbol{u}}|_{\bar{z}=0} = \boldsymbol{0}$, and (ii) free-shear at the liquid interface, $\partial \bar{\boldsymbol{u}}/\partial \bar{z}|_{\bar{z}=\bar{h}} = \boldsymbol{0}$. Furthermore, it follows from these boundary conditions that $\bar{u}_z = 0$.

To obtain an analytical solution in the limit of small, but non-negligible values of ϵ, we resort to a regular perturbation expansion of the form

$$\bar{\boldsymbol{u}} = \bar{\boldsymbol{u}}_0 + \epsilon\bar{\boldsymbol{u}}_1 + O(\epsilon^2), \quad \bar{h} = \bar{h}_0 + \epsilon\bar{h}_1 + O(\epsilon^2) \quad \text{and}$$

$$\bar{p} = \bar{p}_0 + \epsilon\bar{p}_1 + O(\epsilon^2). \tag{5}$$

We truncate the expansion at $O(\epsilon)$, the leading-order inertial term. The subscript 0 denotes $O(1)$ terms (Stokes flow) and 1 denotes $O(\epsilon)$ terms (inertial correction). The expansion in (5) is the weak-inertial correction that is used in a variety of problems to determine the influence of inertia in moderate Re_l flows. Substituting (5) in the Navier-Stokes equation (3) gives the governing equation for the zeroth and first-order problems:

$$O(1) : \frac{\partial^2 \bar{\boldsymbol{u}}_0}{\partial \bar{z}^2} = \bar{\boldsymbol{\nabla}}\bar{p}_0, \tag{6a}$$

$$O(\epsilon) : \frac{\partial^2 \bar{\boldsymbol{u}}_1}{\partial \bar{z}^2} = \bar{\boldsymbol{\nabla}}\bar{p}_1 + (\bar{\boldsymbol{u}}_0 \cdot \bar{\boldsymbol{\nabla}})\bar{\boldsymbol{u}}_0. \tag{6b}$$

Next, we use the expansion (5) in the boundary conditions. It is straightforward to obtain the no-slip conditions at the respective order:

$$O(1) : \bar{\boldsymbol{u}}_0|_{\bar{z}=0} = \boldsymbol{0}, \tag{7a}$$

$$O(\epsilon) : \bar{\boldsymbol{u}}_1|_{\bar{z}=0} = \boldsymbol{0}. \tag{7b}$$

To write the free-shear boundary condition at the liquid interface $\bar{z} = \bar{h} = \bar{h}_0 + \epsilon\bar{h}_1$, we use the *method of domain perturbations* [27]. This method involves expanding a given function in Taylor series near the perturbed boundary. Thus, at $\bar{z} = \bar{h}_0 + \epsilon\bar{h}_1$, we have

$$\frac{\partial \bar{\boldsymbol{u}}}{\partial \bar{z}}\bigg|_{\bar{z}=\bar{h}} = \frac{\partial \bar{\boldsymbol{u}}}{\partial \bar{z}}\bigg|_{\bar{z}=\bar{h}_0} + \epsilon\bar{h}_1 \frac{\partial^2 \bar{\boldsymbol{u}}}{\partial \bar{z}^2}\bigg|_{\bar{z}=\bar{h}_0} + O(\epsilon^2)$$

$$= \frac{\partial \bar{\boldsymbol{u}}_0}{\partial \bar{z}}\bigg|_{\bar{z}=\bar{h}_0} + \epsilon\left(\frac{\partial \bar{\boldsymbol{u}}_1}{\partial \bar{z}} + \bar{h}_1 \frac{\partial^2 \bar{\boldsymbol{u}}_0}{\partial \bar{z}^2}\right)\bigg|_{\bar{z}=\bar{h}_0} + O(\epsilon^2). \tag{8}$$

The final expression was obtained using the expansion (5). The free-shear condition at the respective order is then

$$O(1) : \frac{\partial \bar{\boldsymbol{u}}_0}{\partial \bar{z}}\bigg|_{\bar{z}=\bar{h}_0} = \boldsymbol{0}, \tag{9a}$$

$$O(\epsilon) : \frac{\partial \bar{\boldsymbol{u}}_1}{\partial \bar{z}}\bigg|_{\bar{z}=\bar{h}_0} = -\bar{h}_1 \frac{\partial^2 \bar{\boldsymbol{u}}_0}{\partial \bar{z}^2}\bigg|_{\bar{z}=\bar{h}_0} = -\bar{h}_1 \bar{\boldsymbol{\nabla}}\bar{p}_0|_{\bar{z}=\bar{h}_0}. \tag{9b}$$

We are finally at a stage where we can solve the governing equations and boundary conditions at their respective orders. At the zeroth order, we have the classical lubrication theory, which includes the Stokes equation (6a) and the boundary conditions (7a) and (9a). Solving for $\bar{\boldsymbol{u}}_0$, we get

$$\bar{\boldsymbol{u}}_0 = \frac{\bar{z}}{2}(\bar{z} - 2\bar{h}_0)\bar{\boldsymbol{\nabla}}\bar{p}_0. \tag{10}$$

Next, we substitute (10) in the first-order governing equation (6b) and the boundary conditions (7b) and (9b), and subsequently solve for $\bar{\boldsymbol{u}}_1$:

$$\bar{\boldsymbol{u}}_1 = \frac{\bar{z}}{2}(\bar{z} - 2\bar{h}_0)\bar{\boldsymbol{\nabla}}\bar{p}_1 - \bar{z}\bar{h}_1\bar{\boldsymbol{\nabla}}\bar{p}_0 + \frac{\bar{z}}{120}\left(\bar{z}^5 - 6\bar{h}_0\bar{z}^4 + 10\bar{h}_0^2\bar{z}^3 - 16\bar{h}_0^5\right)\bar{\boldsymbol{\nabla}}\bar{p}_0 \cdot \bar{\boldsymbol{\nabla}}\bar{\boldsymbol{\nabla}}\bar{p}_0. \tag{11}$$

Equation (11) introduces the inertial correction to the well-known Poiseuille flow profile of the Stokes solution (10). One can factor out the z dependence in these equations by computing the depth-averaged flow field, $\bar{\boldsymbol{U}}(x, y) = \bar{h}^{-1} \int_0^{\bar{h}} \bar{\boldsymbol{u}} \, d\bar{z}$. Substituting (5) gives the depth-averaged flow field of the form $\bar{\boldsymbol{U}} = \bar{\boldsymbol{U}}_0 + \epsilon \bar{\boldsymbol{U}}_1 + O(\epsilon^2)$, where

$$\bar{\boldsymbol{U}}_0 = \frac{1}{\bar{h}_0} \int_0^{\bar{h}_0} \bar{\boldsymbol{u}}_0 \, d\bar{z}, \tag{12}$$

$$\bar{\boldsymbol{U}}_1 = \frac{1}{\bar{h}_0} \left(\int_0^{\bar{h}_0} \bar{\boldsymbol{u}}_1 \, d\bar{z} + \frac{1}{\epsilon} \int_{\bar{h}_0}^{\bar{h}_0 + \epsilon \bar{h}_1} \bar{\boldsymbol{u}}_0 \, d\bar{z} - \frac{\bar{h}_1}{\bar{h}_0} \int_0^{\bar{h}_0} \bar{\boldsymbol{u}}_0 \, d\bar{z} \right). \tag{13}$$

Applying (10) and (11) in the above integrals and evaluating, we obtain

$$\bar{\boldsymbol{U}}_0 = \frac{-\bar{h}_0^{\,2}}{3} \bar{\boldsymbol{\nabla}} \bar{p}_0, \quad \bar{\boldsymbol{U}}_1 = \frac{-\bar{h}_0^2}{3} \left(\bar{\boldsymbol{\nabla}} \bar{p}_1 + \frac{2\bar{h}_1}{\bar{h}_0} \bar{\boldsymbol{\nabla}} \bar{p}_0 + \frac{54}{35} (\bar{\boldsymbol{U}}_0 \cdot \bar{\boldsymbol{\nabla}}) \bar{\boldsymbol{U}}_0 \right). \tag{14}$$

We can simplify the above expressions by determining the pressure field. Noting that the pressure is independent of $\bar{z}$ [from (4)], and is simply the dimensionless Laplace pressure:

$$\bar{p}(\bar{x}, \bar{y}) = -\mathrm{Ca}^{-1} \delta^3 \bar{\Delta} \bar{h}(\bar{x}, \bar{y}), \tag{15}$$

where $\mathrm{Ca} = \eta V / \gamma$ is the capillary number. Since the pressure gradient has to balance the viscous stress at the leading order [see (6a)], we have $\delta \sim \mathrm{Ca}^{1/3}$. Disregarding the proportionality constant as done in the classical Stokes flow problem [16,17], we get

$$\delta = \mathrm{Ca}^{1/3} \Rightarrow \epsilon = \mathrm{Ca}^{2/3} \, \mathrm{Re}_l. \tag{16}$$

Thus, by substituting (5) in (15) and collecting terms of the same asymptotic order, we get

$$O(1) : \bar{p}_0(\bar{x}, \bar{y}) = -\bar{\Delta} \bar{h}_0, \tag{17a}$$

$$O(\epsilon) : \bar{p}_1(\bar{x}, \bar{y}) = -\bar{\Delta} \bar{h}_1. \tag{17b}$$

The above expressions can be used in (14) to write $\bar{\boldsymbol{U}}_0$ and $\bar{\boldsymbol{U}}_1$ explicitly in terms of $\bar{h}_0$ and $\bar{h}_1$ alone:

$$\bar{\boldsymbol{U}}_0 = \frac{\bar{h}_0^2}{3} \bar{\boldsymbol{\nabla}} (\bar{\Delta} \bar{h}_0), \tag{18a}$$

$$\bar{\boldsymbol{U}}_1 = \frac{\bar{h}_0^2}{3} \left(\bar{\boldsymbol{\nabla}} (\bar{\Delta} \bar{h}_1) + \frac{2\bar{h}_1}{\bar{h}_0} \bar{\boldsymbol{\nabla}} (\bar{\Delta} \bar{h}_0) - \frac{54}{35} (\bar{\boldsymbol{U}}_0 \cdot \bar{\boldsymbol{\nabla}}) \bar{\boldsymbol{U}}_0 \right). \tag{18b}$$

B. Mass conservation

In addition to the momentum conservation described in Sec. II A, it is necessary for the flow field to satisfy mass conservation given by

$$\frac{\partial \bar{h}}{\partial \bar{t}} + \bar{\boldsymbol{\nabla}} \cdot (\bar{h} \bar{U}) = 0. \tag{19}$$

In the laboratory frame-of-reference, a drop moving in the positive x-axis with a (dimensionless) unit velocity has $\partial \bar{h} / \partial \bar{t} = -\partial \bar{h} / \partial \bar{x}$. Using this relation and the expansion (5), we obtain the kinematic equation of the moving interface at each order:

$$O(1) : -\frac{\partial \bar{h}_0}{\partial \bar{x}} + \bar{\boldsymbol{\nabla}} \cdot (\bar{h}_0 \bar{\boldsymbol{U}}_0) = 0, \tag{20a}$$

$$O(\epsilon) : -\frac{\partial \bar{h}_1}{\partial \bar{x}} + \bar{\boldsymbol{\nabla}} \cdot (\bar{h}_0 \bar{\boldsymbol{U}}_1 + \bar{h}_1 \bar{\boldsymbol{U}}_0) = 0. \tag{20b}$$

Note that $\bar{\boldsymbol{U}}_0$, $\bar{\boldsymbol{U}}_1$, $\bar{h}_0$ and $\bar{h}_1$ are yet unknown. However, since these fields are related through (18a) and (18b), we need only solve for the latter two.

III. DETERMINING THE INTERFACE PROFILE

A. Zeroth order solution: Stokes flow

The shape of the interface in the Stokes regime was determined in Limat and Stone [16]. We briefly rederive their results here for completeness. The kinematic equation for the interface at $O(1)$ is given by (20a). Using (18a) in (20a):

$$-3 \, \frac{\partial \bar{h}_0}{\partial \bar{x}} + \mathbf{\nabla} \cdot \left(\bar{h}_0^3 \bar{\mathbf{\nabla}}(\bar{\Delta} \bar{h}_0) \right) = 0. \tag{21}$$

Using a self-similarity ansatz, the solution is of the form:

$$\bar{h}_0(\bar{x}, \zeta) = \bar{x} \, H(\zeta), \tag{22}$$

where $\zeta = y/x$ [16]. Substituting (22) in (21), one arrives at the ordinary differential equation:

$$\zeta H' - H + H^3 \, (f_x - \zeta f_x{}' + f_y{}') + 3H^2 H'(-\zeta f_x + f_y) = 0, \tag{23}$$

where the prime ($\bullet'$) denotes derivative with respect to ζ. The components of the vector $\boldsymbol{f}(\zeta) = (f_x(\zeta), f_y(\zeta))$ are given by:

$$f_x(\zeta) = -\tfrac{1}{3}((1 + 3\zeta^2)H'' + \zeta(1 + \zeta^2)H'''), \tag{24a}$$

$$f_y(\zeta) = \tfrac{1}{3}(2\zeta H'' + (1 + \zeta^2)H'''). \tag{24b}$$

Equation (23) is a boundary value problem (BVP) that requires four boundary conditions to obtain a unique solution for $H(\zeta)$. By recognizing that the drop is symmetrical about its center line ($\zeta = 0$), we get the first two conditions namely $H'(0) = H'''(0) = 0$. Next, we have at the contact lines $\zeta = \zeta_c$ (given), the height of the drop is zero i.e., $H(\zeta_c) = 0$. The final condition requires no flux penetrating the contact line, i.e., the net flux through any given cross-section of the drop should be zero. $H(0)$ can be determined iteratively such that the no-flux condition is satisfied. However, the solution is extremely stiff near $\zeta = \zeta_c$ and convergence of the BVP would entail using special routines.

So instead, we use an iterative procedure, following Limat and Stone [16] and solve for an initial value problem (IVP). The value of $H(0)$ is first arbitrarily assigned. Note however that since $H(\zeta)$ relates directly to the height of the liquid interface, negative values are physically irrelevant and hence excluded. Next, we have $H'(0) = H'''(0) = 0$ as before due to symmetry. Finally, based on a particular choice of $H''(0)$, one can solve the IVP to obtain multiple solutions for $H(\zeta)$, out of which some do not have a root [see Fig. 8(a)]. In other words, the drop interface does not meet the solid and form a contact line. These are not physically relevant solutions and may be discarded. However, there also exist multiple solutions of $H(\zeta)$ that have roots. The correct choice of $H''(0)$ is then the one that also obeys the no-flux condition at the contact line. Some of these valid solutions of $H(\zeta)$ for the initial conditions $H(0)$ and $H''(0)$ tabulated in Table I are shown in Fig. 2(a); they yield unique values of ζ_c. For example, when $H(0) = 1.215$, the choice $H''(0) = -2.623$ satisfies the zero net flux condition as shown in Figs. 8(b) and 8(c). This solution places the contact line along $\zeta = \zeta_c = 1$ (up to four digits of precision) which corresponds to an opening angle $\phi = \tan^{-1}(\zeta_c) = 45°$. Solving the IVP using Table I as seed is faster and more stable than solving the BVP.

B. First-order solution: Inertial correction

To determine the leading-order inertial correction, we use the mass conservation equation at $O(\epsilon)$. Substituting (18a) and (18b) in (20b), we obtain the differential equation for the correction to the interface profile, $\bar{h}_1$:

$$-3 \, \frac{\partial \bar{h}_1}{\partial \bar{x}} + \bar{\mathbf{\nabla}} \cdot \left(\bar{h}_0^3 \bar{\mathbf{\nabla}}(\bar{\Delta} \bar{h}_1) + 3\bar{h}_0^2 \bar{h}_1 \bar{\mathbf{\nabla}}(\bar{\Delta} \bar{h}_0) - \frac{54}{35} \, \bar{h}_0^3 (\bar{\boldsymbol{U}}_0 \cdot \bar{\mathbf{\nabla}})\bar{\boldsymbol{U}}_0 \right) = 0 \tag{25}$$
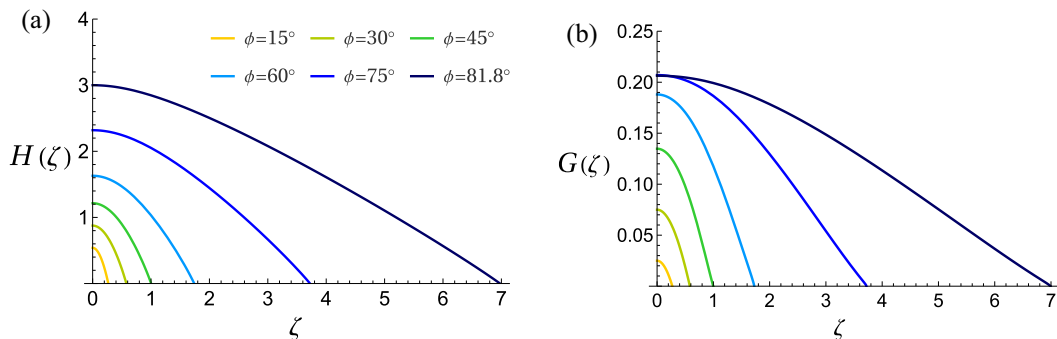
FIG. 2. Valid solutions of (a) Eq. (23) and (b) Eq. (27) for various corner semiopening angle, ϕ. For small ϕ, the curves can be approximated as parabolas (see Appendix B). Note that the plots are symmetrical about the y axis for negative values of ζ.

with $\boldsymbol{U}_0$ given in (18a). Keeping in mind (22), a quick examination of this equation reveals that it admits a self-similar solution of the form:

$$\bar{h}_1(\bar{x}, \zeta) = \bar{x}^2\, G(\zeta), \tag{26}$$

with $\zeta = y/x$. Substituting the expressions for h_0 and h_1 from (22) and (26), respectively, in (25), we arrive at

$$\zeta G' - 2G + 2H^2(g_x + Gf_x) - \zeta(H^2(g_x + Gf_x))' + (H^2(g_y + Gf_y))' = 0, \tag{27}$$

where the vector $\boldsymbol{f}(\zeta) = (f_x(\zeta), f_y(\zeta))$ is given in (24a), (24b) and $\boldsymbol{g}(\zeta) = (g_x(\zeta), g_y(\zeta))$ is

$$g_x(\zeta) = \frac{1}{3}\left(6Gf_x + \frac{54}{35}H^4(\zeta f_x - f_y)(2H'f_x + Hf_x') - \zeta(1 + \zeta^2)HG'''\right), \tag{28a}$$

$$g_y(\zeta) = \frac{1}{3}\left(6Gf_y + \frac{54}{35}H^4(\zeta f_x - f_y)(2H'f_y + Hf_y') + (1 + \zeta^2)HG'''\right). \tag{28b}$$

Note that $H(\zeta)$ is the Stokes solution for a contact line at some $\zeta = \zeta_c$, and is known at this stage from Sec. III A. Equation (27) has to be supplemented with four boundary conditions to obtain a unique solution for $G(\zeta)$. The symmetry of the drop automatically lets us assign $G'(0) = 0$ and $G'''(0) = 0$. Next, we note that the height of the interface should be zero at the contact line $\zeta = \zeta_c$ and this constraint sets $G(\zeta_c) = 0$. The final boundary condition is obtained by specifying the value of $G''(0)$ (or $G(0)$). However, choosing any arbitrary value is not sufficient. Similar to the Stokes flow problem, the correct choice should result in a net zero-flux at any point on the contact line and through any cross-section of the drop (see Appendix C). The unique solutions of $G(\zeta)$ for a few specified values of ζ_c (or equivalently, the opening angle ϕ) are shown in Fig. 2(b); the corresponding choice of values of $G''(0)$ are also listed in Table I in the Appendix. In the example considered in Sec. III A (drop having opening angle $\phi = 45°$ ($\zeta_c = 1$)), the correct choice of $G''(0) = -0.29$.

There are a few observations that need to be made here: First, $G(\zeta)$ directly relates to the *correction* in the interface height due to inertia and so, it is allowed to assume negative values. Even so, it is interesting to note that the valid solution is always positive for the wide range of opening angles shown here. One can analytically show that it is always positive in the asymptotic limit of small opening angles (see Appendix B). Second, $G(0)$ increases with the opening angle until about $\phi \approx 75°$, beyond which it seems to saturate, rendering the solution sensitive to the choice of $G(0)$. For this reason, opting $G''(0)$ as the boundary condition is a more reliable alternative. We provide the approximate values of $G(0)$ and $G''(0)$ for a few opening angles in Table I.

IV. RESULTS

We can now use the solutions for $H(\zeta)$ and $G(\zeta)$ obtained in Sec. III for various corner opening angles to determine the inertia-corrected interface profile and flow fields. Inspired by the experiments of Puthenveettil *et al.*, [7], we shall use the properties of water and mercury as examples to quantify our findings because the drops of these liquids move in the inertial regime when their receding contact line destabilizes. At room temperature, the (density, surface tension, and dynamic viscosity) of water and mercury are $(\rho_w = 10^3 \text{ kg m}^{-3}; \gamma_w = 7 \times 10^{-2} \text{ N m}^{-1}; \eta_w = 10^{-3} \text{ Pa s})$ and $(\rho_m = 10^4 \text{ kg m}^{-3}; \gamma_m = 5 \times 10^{-1} \text{ N m}^{-1}; \eta_m = 1.5 \times 10^{-3} \text{ Pa s})$, respectively. Water and mercury have critical capillary numbers of $\text{Ca}_{cr} \approx 4 \times 10^{-3}$ and $\text{Ca}_{cr} \approx 1.5 \times 10^{-3}$ [7].

Before we proceed, it is useful to define a local Reynolds number based on the dimensional distance x from the corner, given by $\text{Re}_x = xV\rho/\eta = \bar{x} \text{ Re}_l$. Also note that one can relate Re_x to the capillary number via $\text{Re}_x = \text{Ca} \, x/l_{vc}$, where $l_{vc} = \eta^2/(\gamma \rho)$ is the viscocapillary length of the liquid. For mercury and water, $l_{vc} \sim 10^{-4}$ μm and $l_{vc} \sim 10^{-2}$ μm, respectively.

A. Interface profile

The liquid interface is obtained by substituting the expressions for h_0 and h_1 from (22) and (26):

$$\bar{h}(\bar{x}, \zeta) = \bar{x} H(\zeta) + \epsilon \bar{x}^2 G(\zeta) + O(\epsilon^2). \tag{29}$$

Truncating at $O(\epsilon)$ and writing in dimensional form by using (16), we get

$$h(x, \zeta) = \text{Ca}^{1/3} x H(\zeta) + \text{Ca Re}_x x G(\zeta). \tag{30}$$

Note that Ca Re_x together is the local Weber number. The first term in (30) is the Stokes solution, with the classical $\text{Ca}^{1/3}$ scaling for partially wetting liquids [16,28]. By rewriting $\text{Re}_x = \text{Ca} \, x/l_{vc}$, we see that the leading-order inertial term obeys a Ca^2 scaling.

We have seen in Sec. III B that the solutions that satisfy the no-flux condition have $G(\zeta) \geqslant 0$ for all opening angles. Thus, the inertial correction in (30) is always positive, which implies that the height of every point of the Stokes interface is increased due to inertia. A similar enhancement in the height of the liquid interface because of inertia has been reported previously for the Landau-Levich (fully wetting) problem [22]. In the Stokes limit, the interface height scales linearly with x, giving it a conical structure, as shown by the dashed lines in Fig. 3. Since Re_x varies linearly with x, the inertial correction in (30) has a quadratic dependence with x. Indeed, we see its implication in the example shown in Fig. 3, where the resulting surface has a cusplike geometry. Formation of cusps has also been reported in experiments at high contact line speeds, indicating that inertia might be playing an important role in the corner-to-cusp transition of moving contact lines [3,6,7].

A useful quantification is the side angle of the drop, θ_x. It is the internal angle in the xz plane defined at a distance x along the centerline ($\zeta = 0$). A schematic of this side angle is shown in Fig. 3 (inset). It is formally defined as

$$\tan\theta_x = \left.\frac{\partial h}{\partial x}\right|_{\zeta=0} = \text{Ca}^{1/3}H(0) + 2\text{Ca Re}_x G(0). \tag{31}$$

For a given semiopening angle ϕ, the side angle is a constant θ_0 in the case of Stokes flow. However, by including inertial effects, we see that the side angle θ_x increases with the distance from the corner as well. To evaluate the side angle using (31), one can utilize Table I, which lists the values of $H(0)$ and $G(0)$ for different opening angles. Figure 4(a) shows this variation for various opening angles.

For small opening angles ($\phi \rightarrow 0$), one can show that the cross-section profile of the interface is parabolic, similar to the noninertial case (see Appendix B). Furthermore, in this case, we have the approximation $H(0)^3 \sim \tan^2\phi$ and $G(0) \sim \tan^2\phi$, giving us the $\theta - \phi$ relation in (B7), valid for small ϕ. To facilitate comparison with other works in literature and experiments (see [29]), we take the cube of this expression and truncate it at the leading order in $\text{Ca}^{2/3}\text{Re}_x(\ll 1)$ to get the
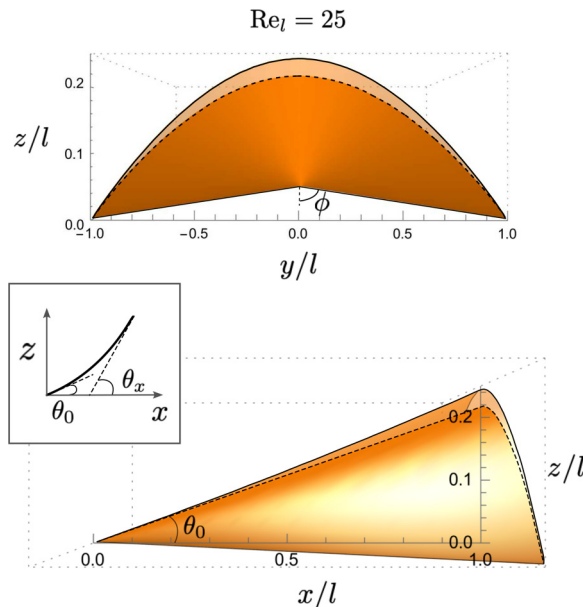
FIG. 3. Front and side profiles of the liquid interface for a semiopening angle of $\phi = 45°$ ($\zeta_c = 1$), Ca $= 5.65 \times 10^{-3}$ and $\text{Re}_l = 25$. The liquid is assumed to have properties of water ($\text{Ca}_{\text{cr}} = 4 \times 10^{-3}$). The Stokes solution (cone) is shown by the dashed line while the inertia-corrected solution (cusp) is shown by the solid line. Inset: a schematic of the side angle θ_x; the true side angle, θ_0, computed at $x = 0$ is the Stokes solution.

inertia-corrected relation:

$$\tan^3 \theta_x \approx \frac{35}{16} \text{Ca} \tan^2 \phi (1 + 2.262 \ \text{Ca}^{2/3} \text{Re}_x \tan^{4/3} \phi). \tag{32}$$

Up until this point, we have not included any contact line dynamics in our model; the opening angle ϕ (or equivalently, ζ_c) was chosen independently. However, it has been observed in experiments that ϕ reduces with increasing Ca such that the velocity of the contact line is maintained at the critical value [1,2]. We account for this variation by including the commonly used phenomenological relation:

$$\sin \phi = \text{Ca}_{\text{cr}}/\text{Ca}, \tag{33}$$

in our model [1,2]. A more detailed mechanism for selection of ϕ was explored in Snoeijer *et al.* [30]. While it is natural to expect inertia to increase with the drop velocity, one should keep in mind that the competing viscous forces also increase due to the corresponding narrowing of the corner. To analyze the nontrivial effects that arise from introducing the contact line dynamics in the model, we shall use mercury and water at room temperature as example liquids. The properties of mercury and water were described at the beginning of this section.

For any specified liquid, since ϕ is enslaved to Ca, there is a unique value of θ_x for a given Ca and distance x from the corner. These values for mercury and water at $x = 10$ μm are highlighted in Fig. 4(a) by crosses and circles, respectively. Since $\text{Re}_x = \text{Ca} \, x/l_{vc}$, θ_x can be expressed entirely in terms of Ca after the inclusion of contact line dynamics, as shown in Fig. 4(b) for some fixed x ($=10$ μm). Contrary to what one might expect from (31), we see that θ_x reduces with Ca, consistent with experimental observations [6,7]. This is due to the stronger influence of the narrowing geometry (decreasing $H(0)$ and $G(0)$ values) compared to increasing Ca. Despite this, we see in Fig. 4(c) that the fractional correction introduced by inertia increases with Ca. Also note
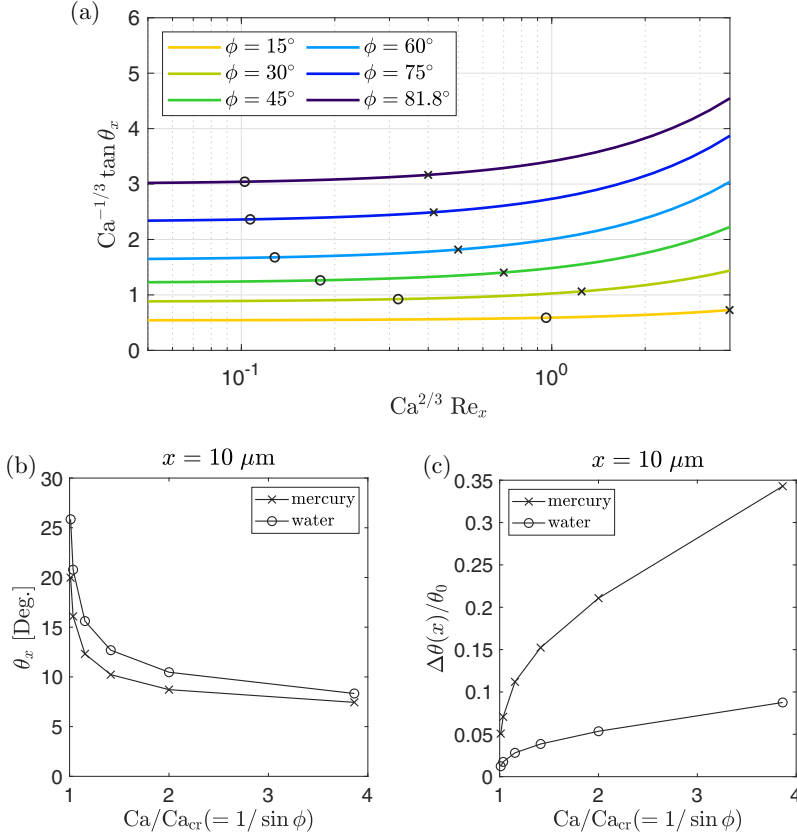
FIG. 4. (a) Variation of the side angle θ_x due to inertia given by (31) for various corner semiopening angles. The cross and circle markers denote the values that get selected when using contact line dynamics (33) for mercury and water, respectively, at $x = 10$ μm. (b) Same as markers in (a) but plotted solely against Ca. (c) The fractional correction $\Delta\theta_x/\theta_0 = (\theta_x(x) - \theta_0)/\theta_0$ in the side angle due to inertia.

that the correction for mercury is higher than water in spite of the former's smaller Ca_{cr}, due to its much higher Re_x values (at $x = 10$ μm, $Re_x \sim O(1)$ for water and $Re_x \sim O(10)$ for mercury).

B. Depth-averaged flow field

Using the interface profile determined in the previous section, one can compute the pressure fields using (17a). At the zeroth and first orders, these are, respectively, (in dimensionless form)

$$\bar{p}_0 = -\frac{(1 + \zeta^2)}{\bar{x}} H''(\zeta), \quad \text{and} \tag{34}$$

$$\bar{p}_1 = -(1 + \zeta^2)G''(\zeta) + 2\zeta G'(\zeta) - 2G(\zeta). \tag{35}$$

Note that when approaching the corner, $\bar{x} \to 0$, the Stokes flow pressure $\bar{p}_0$ becomes singular, whereas the inertial correction $\bar{p}_1$ does not. This is unlike the case of a straight contact line, where the leading-order stress from inertia exhibits a logarithmic singularity [21].

The depth-averaged velocity field at the zeroth order (Stokes flow) is obtained by substituting (22) in (18a):
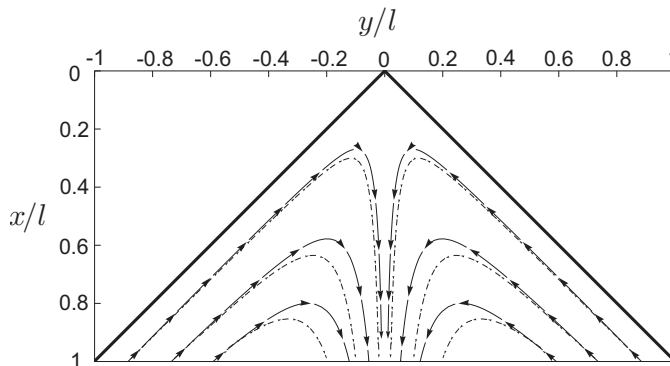
$$\bar{\boldsymbol{U}}_0(\zeta) = H(\zeta)^2 \boldsymbol{f}(\zeta) \tag{36}$$

FIG. 5. Streamlines of the depth-averaged flow near the corner shown in the reference frame of the moving drop i.e., $(\boldsymbol{U} - \boldsymbol{V})/V$, obeying (38). The dashed lines are the Stokes solution while the solid lines are the inertia-corrected solution. A semiopening angle of $\phi = 45°$ and $\mathrm{Ca} = 5.65 \times 10^{-3}$ is chosen to mimic water ($\mathrm{Ca}_{\mathrm{cr}} = 4 \times 10^{-3}$). The local Reynolds number at some $x = l$ is taken to be $\mathrm{Re}_l = 25$. For water, $l \approx 250$ μm.

with $\boldsymbol{f}(\zeta)$ given in (24a), (24b). Likewise, at the first order, we get by substituting (22), (26), and (36) in (18b):

$$\bar{\boldsymbol{U}}_1(\bar{x}, \zeta) = \bar{x}\, H(\zeta)\boldsymbol{g}(\zeta) \tag{37}$$

with $\boldsymbol{g}(\zeta)$ given in (28a), (28b). Thus, the total flow velocity is then $\bar{\boldsymbol{U}}(\bar{x}, \zeta) = \bar{\boldsymbol{U}}_0(\zeta) + \epsilon\bar{\boldsymbol{U}}_1(\bar{x}, \zeta) + O(\epsilon^2)$. In dimensional form, this is

$$\frac{\boldsymbol{U}(x, \zeta)}{V} = H(\zeta)^2\boldsymbol{f}(\zeta) + \mathrm{Ca}^{2/3}\mathrm{Re}_x\, H(\zeta)\boldsymbol{g}(\zeta). \tag{38}$$

We remind the reader that $\boldsymbol{U} = (U_x, U_y)$ is the local depth-averaged velocity field within the liquid, and is different from the velocity of the contact line, $\boldsymbol{V} = (V, 0)$. The Stokes velocity field depends only on the semiopening angle, ϕ, while the inertial correction depends on ϕ, Ca and distance from the corner, x. Furthermore, since $\mathrm{Re}_x = \mathrm{Ca}\, x/l_{vc}$, the leading-order inertial term scales as $\mathrm{Ca}^{5/3}$.

In Fig. 5, we show as an example, the Stokes and inertia-corrected streamlines in the reference frame of a moving drop. One can make the following qualitative observation, true for all opening angles: The fluid approaching the corner is forced further toward it due to the inertia. After turning the corner, the fluid accelerates away from it, and at the same time, is drawn further toward the centerline of the drop ($\zeta = 0$). The flow velocity is maximum along this centerline.

To get a quantitative estimate of the effect of inertia, we compute the centerline velocity, where the depth-averaged flow is strictly along the x axis i.e., $U^c(x) = U_x(x, 0)$. It is determined using (38) where the values of $H(0)$, $f_x(0)$ and $g_x(0)$ for a few opening angles can be read off from Table I. Note that $f_y(0)$ and $g_y(0)$ are strictly zero. The results are shown in Fig. 6(a) for various semiopening angles, ϕ. One can see immediately that the centerline velocity is more than the drop velocity i.e., $U^c/V > 1$, even in the Stokes limit ($\mathrm{Re}_x \to 0$). With the inclusion of the inertial correction, this value increases with Re_x, for all opening angles. Thus, we conclude that for a given drop velocity, the flow velocity increases with the distance from the corner due to inertia. The magnitude of this increase (i.e., the slope of the curve) depends on the opening angle, with the most increase seen for intermediate values.

We did not include any contact line dynamics for generating Fig. 6(a), which is to say that ϕ and Ca were treated as independent parameters. To get a more practical picture, we shall now include the phenomenological relation between these two quantities given by (33), as we did in the previous section for the side angle. The values of U^c/V that get selected in this manner for two example liquids viz. mercury and water at $x = 10$ μm are shown with crosses and circles,
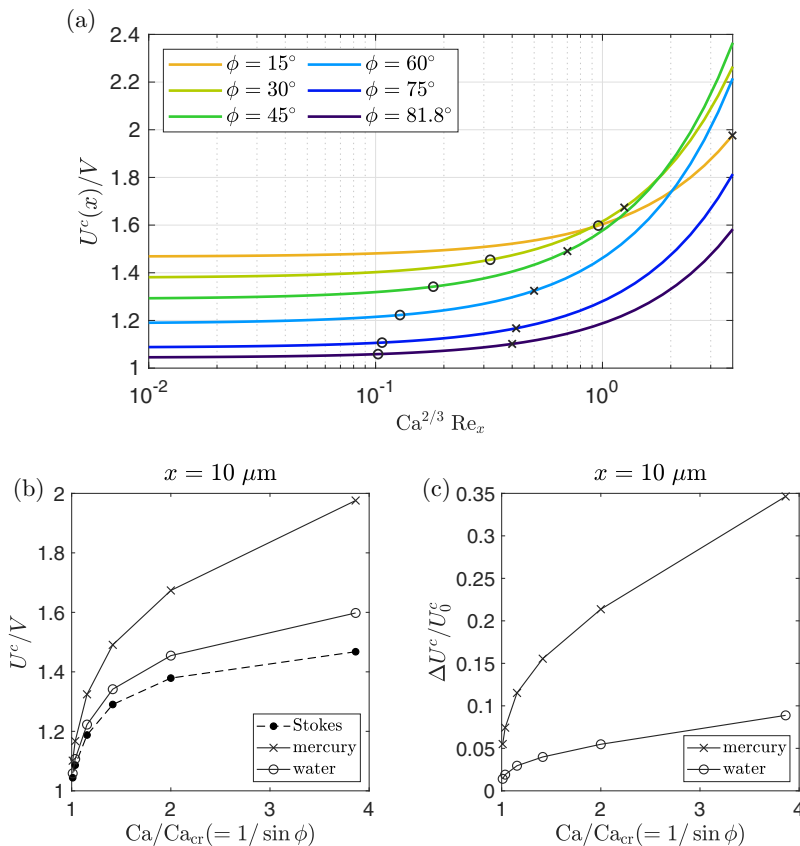
FIG. 6. (a) Variation of the centerline velocity due to inertia given by (38) for various corner semiopening angles. The cross and circle markers denote the values that get selected when using contact line dynamics (33) for mercury and water, respectively, at $x = 10$ μm. (b) Same as markers in (a) but plotted solely against Ca. (c) The fractional correction $\Delta U^c/U_0^c = (U^c(x) - U_0^c)/U_0^c$ in the centerline velocity due to inertia.

respectively. We show these explicitly in terms of the Ca in Fig. 6(b). Notably, the Stokes centerline velocity, U_0^c/V, being a function only of ϕ, is given by a universal curve for all liquids and at any distance from the corner. The inertia-corrected velocities for both mercury and water at some $x(=10$ μm here) are not only higher than the Stokes velocity, as mentioned, but they also increase with Ca. In comparison, the centerline velocity of mercury is much higher than water at any distance from the corner because of the higher local Reynolds number of the former. Figure 6(c) shows the fractional correction introduced by inertia at $x = 10$ μm which also increases with Ca. This implies that inertia overshadows the enhanced viscous dissipation caused by the narrowing of the corner at higher speeds.

V. SUMMARY AND DISCUSSIONS

We studied the effect of inertia in receding contact lines of partially wetting liquids beyond their critical capillary number when they destabilize and form a corner. To this end, we modeled the flow field near the contact line using thin-film equations, as is classically done, but retained the convective (inertial) term. The leading-order inertial contribution is obtained by linearizing the equations using a regular perturbation expansion. Inertial effects are found to be significant when $Ca^{2/3}Re_x \gtrsim 1$, where Re_x is the local Reynolds number based on the distance from the corner, x.

For destabilized contact lines of many common liquids, including mercury and water considered here, $\mathrm{Ca} \sim 10^{-3} - 10^{-2}$. This implies that inertia becomes significant when $\mathrm{Re}_x \gtrsim 10 - 10^2$, which corresponds to experimentally relevant length scales of $x \sim 10 - 100$ μm for mercury and $x \sim 100 - 1000$ μm for water. Gravitational effects can be ignored as these distances fall well within their respective capillary lengths.

In the Stokes regime, the thin-film equations predict the receding contact line to be of a conical structure with a self-similar flow within [16,17]. Here, we have provided a leading-order inertial correction to this solution, which is also self-similar. We have also shown that for all corner opening angles, inertia enhances the interface height. A similar enhancement in the liquid film thickness by inertia was reported in the fully wetting case (Landau-Levich problem) [22,23]. Furthermore, the leading-order inertial correction in our case was found to scale linearly with the local Weber number ($\mathrm{We}_x = \mathrm{Ca}\,\mathrm{Re}_x$), giving rise to a cusplike shape of the interface for all corner opening angles. However, note that in computing the correction, we assumed the contact line to remain a straightedged corner (ϕ independent of x), which is not true in general, as experiments report a corner-to-cusp transition of contact lines at high speeds [6,7].

To understand the inertial effects on the flow field, we computed the depth-averaged velocity near the contact line. The inertial correction was found to scale as $\mathrm{Ca}^{5/3}$ at a given distance from the corner. We also found that inertia increases the fluid influx from the bulk and forces the flow further toward the corner. Consequently, this enhances the outflux through the centerline of the drop for all corner opening angles.

We then introduced contact line dynamics in our model using a simple phenomenological relation for the corner opening angle, viz. $\sin\phi = \mathrm{Ca}_{\mathrm{cr}}/\mathrm{Ca}$ [1], which is to say that increasing Ca reduces the opening angle. In doing so, we introduced a competition between the increased drop speed and the corner confinement on the flow; the former enhances the fluid inertia while the latter suppresses it. Interestingly, we found that despite this competition, there is an overall increase in the inertial contribution with an increase in Ca. We have shown this numerically by taking contact lines of water and mercury as examples. While these are theoretical estimates, note that in practice, the cornered end undergoes either a pearling instability or forms a rivulet when $\phi \ll 1$. In experiments, it happens around $\phi = \pi/6$ or $30°$ [3,7]. In future works, it would be interesting to see how inertia itself affects this instability [30].

While the assumption of ϵ ($=\mathrm{Ca}^{2/3}\mathrm{Re}_l$) $\ll 1$ was used to obtain a perturbative correction to the Stokes solution, the asymptotic expansion is valid numerically even for $\epsilon \sim O(1)$. For fast motion of contact lines, $\epsilon \gg 1$, the flow develops a viscous boundary layer close to the surface. In such cases, the use of boundary layer theory instead has been shown to agree well with experiments [7].

The Stokes flow stresses diverge as $1/x$ when approaching the corner, $x \to 0$ [see (34)]. It has been observed in experiments that the corner rounds off around the viscocapillary length, l_{vc}, to regularize this corner singularity [31]. Additional contact line physics can be implemented in the model to capture this fine tip structure [31], although no such regularization was used in the present work. This makes our analysis less suitable for comparison with experiments when $x \lesssim l_{vc}$. Furthermore, far away from the corner, our analysis is not valid close to and beyond the capillary length, l_c, where gravitational effects become important. Thus, it is best applicable in $l_{vc} \ll x \ll l_c$.

The inertial correction provided in the present work cannot be applied to advancing contact lines because of the large capillary numbers at which destabilization occurs ($\mathrm{Ca}_{\mathrm{cr}} \sim O(10)$), accompanied by a large interface deformation [5]. However, it remains relevant for addressing problems concerning destabilized receding contact lines, both from a fundamental standpoint as well as in many industrial processes operating at moderately large Reynolds numbers [5,11,12].

TABLE I. The centerline values ($\zeta = 0$) for various semiopening angles, ϕ (or equivalently, $\zeta_c(= \tan\phi)$) used in the main text.

ϕ [Deg.], ζ_c	$H(0)$	$H''(0)$	$G(0)$	$G''(0)$	$f_x(0)$	$g_x(0)$
15, 0.27	0.54	-15.1	0.025	-0.68	5.033	0.2517
30, 0.58	0.876	-5.39	0.075	-0.458	1.797	0.2695
45, 1	1.215	-2.62	0.1355	-0.29	0.874	0.237
60, 1.73	1.63	-1.34	0.185	-0.138	0.447	0.168
75, 3.73	2.319	-0.606	0.207	-0.039	0.202	0.0836
81.8, 6.94	3	-0.348	0.2064	-0.0136	0.116	0.0479

APPENDIX A: VALUES AT CENTERLINE OF THE DROP

One can use Table I, for example, to determine the magnitude of the centerline depth-averaged velocity of the drop given by $U^c/V = H(0)^2 f_x(0) + \mathrm{Ca}^{2/3}\mathrm{Re}_x H(0)g_x(0)$ or the side angle in (31).

APPENDIX B: APPROXIMATION FOR SMALL OPENING ANGLES

The functions $H(\zeta)$ and $G(\zeta)$ obtained in Sec. III (Fig. 2) are rescaled with their values at the centerline ($\zeta = 0$) in Fig. 7. For small ϕ (equivalently, $\zeta_c \ll 1$), the solutions approximate as a single curve which is a function of ζ/ζ_c. Thus, in these cases, we can write $H(\zeta) = H(0)\hat{H}(\zeta/\zeta_c)$ and $G(\zeta) = G(0)\hat{G}(\zeta/\zeta_c)$, with the properties $\hat{H}(\pm 1) = \hat{G}(\pm 1) = 0$, $\hat{H}(0) = \hat{G}(0) = 1$. In fact, from Fig. 7, we see that the curve is approximately described by a parabola for both $\hat{H}$ and $\hat{G}$

$$\hat{H}(\zeta/\zeta_c) = \hat{G}(\zeta/\zeta_c) \approx 1 - \left(\frac{\zeta}{\zeta_c}\right)^2. \tag{B1}$$

The former is the small-angle approximation given by Limat and Stone [16].

Using (B1) in (24a) and (24b), we get

$$f_x \approx \frac{2(1 + 3\zeta^2)}{3\zeta_c^2}H(0), \quad f_y \approx \frac{-4\zeta}{3\zeta_c^2}H(0), \tag{B2}$$

respectively. By using (B1) and (B2) in the expression for the Stokes flow flux (C5) to satisfy the zero-net flux condition, we get the approximate expression for $H(0)$ given in (B3). Computing g_x and g_y [Eqs. (28a) and (28b)] in a similar fashion, and using it in (C6), we get the net inertial flux,
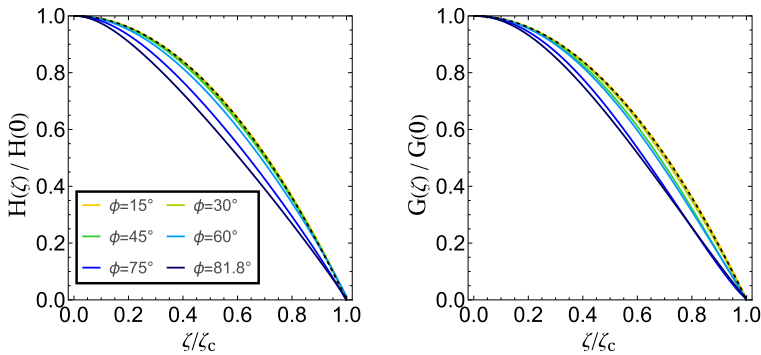

FIG. 7. Rescaled solutions $H(\zeta)$ and $G(\zeta)$ from Fig. 2 for various opening angles, ϕ (or equivalently $\zeta_c = \tan\phi$). Dashed line shows the parabolic curve $1 - (\zeta/\zeta_c)^2$.

which when equated to zero, gives the expression for $G(0)$ in (B4). Thus, for small opening angles i.e., $\zeta_c \ll 1$:

$$H(0) \approx (35/16)^{2/3} \, \zeta_c^{2/3}, \tag{B3}$$

$$G(0) \approx \frac{70}{143} \zeta_c^2 \frac{\left(1 - 9\zeta_c^2/17\right)}{\left(1 + \zeta_c^2/2\right)}, \tag{B4}$$

$$f_x(0) \approx \frac{2}{3\zeta_c^2} H(0), \quad f_y(0) = 0, \tag{B5}$$

$$g_x(0) \approx \frac{4}{3\zeta_c^2} H(0)G(0), \quad g_y(0) = 0. \tag{B6}$$

Since $G(0)$ in (B4) is positive and $\hat{G}(\zeta/\zeta_c)$ is parabolic, the interface profile $G(\zeta)$ is always positive.

Using the above approximation along with the fact that $\zeta_c = \tan\phi$, the $\theta - \phi$ relation in (31) becomes

$$\tan\theta_x \approx \left(\frac{35}{16}\right)^{1/3} \mathrm{Ca}^{1/3} \tan^{2/3}\phi + \frac{140}{143} \, \mathrm{We}_x \tan^2\phi, \tag{B7}$$

where $\mathrm{We}_x = \mathrm{Ca}\,\mathrm{Re}_x$ is the local Weber number.

APPENDIX C: FLUX NEAR THE CONTACT LINE

$\bar{U}$ is the depth-averaged velocity field rescaled by the drop velocity. The relative velocity is then $\bar{U} - \hat{x}$, where $\hat{x}$ is the unit vector in the positive x direction. The dimensionless local flux j_x is then

$$\bar{j}_x = \bar{h}(\bar{U} \cdot \hat{x} - 1). \tag{C1}$$

Like in the rest of the article, expanding $\bar{h} = \bar{h}_0 + \epsilon\bar{h}_1$ and $\bar{U} = \bar{U}_0 + \epsilon\bar{U}_1$ gives $\bar{j}_x = \bar{j}_{0,x} + \epsilon\bar{j}_{1,x} + O(\epsilon^2)$ with

$$\bar{j}_{0,x} = \bar{h}_0(\bar{U}_{0,x} - 1), \tag{C2}$$

$$\bar{j}_{1,x} = \bar{h}_1(\bar{U}_{0,x} - 1) + \bar{h}_0\bar{U}_{1,x}, \tag{C3}$$

where the subscript x denotes the component along the x-direction. The expressions for $\bar{h}_0$, $\bar{h}_1$, $\bar{U}_0$, and $\bar{U}_1$ are given in (22), (26), (36), and (37), respectively. We assume terms of $O(\epsilon^2)$ or higher orders have negligible contribution to the flux. The net flux through a cross-section of the drop at an arbitrary location x is

$$\bar{J}_x = 2 \int_0^{\zeta_c \bar{x}} \bar{j}_x \, d\bar{y}. \tag{C4}$$

Substituting (C2), we obtain the net flux through any cross-section in the Stokes limit, in dimensionless form:

$$O(1): \quad \bar{J}_{0,x} = -2\bar{x}^2 F_0(\zeta_c) \quad \text{where,} \quad F_0(\zeta_c) = \int_0^{\zeta_c} H(1 - H^2 f_x) \, d\zeta. \tag{C5}$$

The zero-net flux condition at this order yields a unique value of $H''(0)$ which solves for $H(\zeta)$ for a given opening angle. For example, when $H(0) = 1.215$, the value of the function F_0 for various $H''(0)$ are shown in Fig. 8. Only $H''(0) = -2.623$ satisfies the zero-net flux condition; the corresponding value of $\zeta_c = 1$ ($\phi = 45°$). Moreover, note that only for this particular choice of $H''(0)$ is the local flux across any point on the contact line also zero ($j_{0,x}(x, \zeta_c) = 0$). The choice of $H(0)$ and $H''(0)$ obtained in this manner for a few values of ϕ are given in Table I.
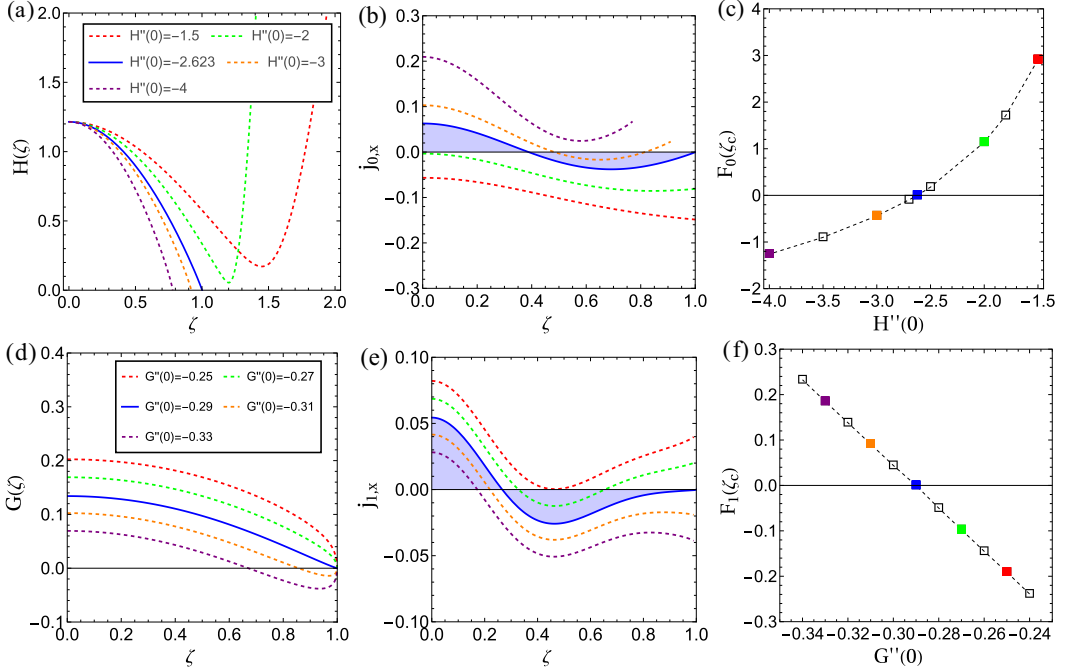
FIG. 8. $O(1)$ Stokes regime: (a) Solutions of (23) with the boundary conditions $H(0) = 1.215$, $H'(0) = H'''(0) = 0$ and for different values of $H''(0)$. The physically valid solution (shown in blue solid line) is decided by the zero-net flux condition through the cross-section (yz plane). (b) Local flux along a cross section; Only $\zeta \geqslant 0$ is shown for reasons of symmetry. The area under each curve represents the net flux through the cross-section. (c) The net flux [Eq. (C5)], shaded area in (b) is proportional to $F_0(\zeta)$, which is shown here for the different values of $H''(0)$. A zero net flux i.e., $F_0(\zeta_c) = 0$, is obtained only for $H''(0) = -2.623$, making it the correct solution, and results in $\zeta_c = 1$ or $\phi = 45°$. $O(\epsilon)$ Inertial correction: (d) Solutions of $G(\zeta)$ in Eq. (23) with the boundary conditions $G(\zeta_c = 1) = 0$, $G'(0) = G'''(0) = 0$ and for different values of $G''(0)$. The correct choice of $G''(0)$ is decided by the zero-net flux condition along any arbitrary cross-section of the drop. (e) Local inertial flux correction; for reasons of symmetry, only $\zeta \geqslant 0$ is shown. The area under each curve represents the net inertial flux through the cross-section. (f) The net inertial flux [Eq. (C6)] is proportional to $F_1(\zeta)$, which is shown here for the different values of $G''(0)$. A zero net flux, i.e., $F_1(\zeta_c = 1) = 0$, is obtained only for $G''(0) = -0.29$, making it the correct choice.

Similarly, the leading-order inertial flux is obtained by substituting (C3) in (C4):

$$O(\epsilon): \quad \bar{J}_{1,x} = -2\bar{x}^3 F_1(\zeta_c), \quad \text{where,} \quad F_1(\zeta_c) = \int_0^{\zeta_c} G(1 - H^2 f_x) - H^2 g_x \, d\zeta. \quad \text{(C6)}$$

The flux at this order $O(\epsilon)$ should also independently vanish in order to satisfy the macroscopic mass-flux condition. This condition should be evoked to determine the correct choice of the boundary conditions. Note that ζ_c is determined from the solution at $O(1)$. In this example, we have $\zeta_c = 1$ (see Fig. 8). Figure 8(d) shows the different values of the boundary condition $G''(0)$ for the case $\zeta_c = 1$ and the correct value which satisfies the zero-flux condition is highlighted. Moreover, note that the local flux across the contact line is also zero ($j_{1,x}(\zeta_c) = 0$) only for this particular choice of $G''(0)$.

[1] T. Blake and K. Ruschak, A maximum speed of wetting, Nature (London) **282**, 489 (1979).

[2] J. G. Petrov and R. V. Sedev, On the existence of a maximum speed of wetting, Colloids Surf. **13**, 313 (1985).

[3] T. Podgorski, J.-M. Flesselles, and L. Limat, Corners, cusps, and pearls in running drops, Phys. Rev. Lett. **87**, 036102 (2001).

[4] J. H. Snoeijer, B. Andreotti, G. Delon, and M. Ferminger, Relaxation of a dewetting contact line. part 1. a full-scale hydrodynamic calculation, J. Fluid Mech. **579**, 63 (2007).

[5] J. H. Snoeijer and B. Andreotti, Moving contact lines: Scales, regimes, and dynamical transitions, Annu. Rev. Fluid Mech. **45**, 269 (2013).

[6] N. Le Grand, A. Daerr, and L. Limat, Shape and motion of drops sliding down an inclined plane, J. Fluid Mech. **541**, 293 (2005).

[7] B. A. Puthenveettil, V. K. Senthilkumar, and E. J. Hopfinger, Motion of drops on inclined surfaces in the inertial regime, J. Fluid Mech. **726**, 26 (2013).

[8] M. He and S. R. Nagel, Characteristic interfacial structure behind a rapidly moving contact line, Phys. Rev. Lett. **122**, 018001 (2019).

[9] E. Vandre, M. S. Carvalho, and S. Kumar, On the mechanism of wetting failure during fluid displacement along a moving substrate, Phys. Fluids **25**, 102103 (2013).

[10] J. S. Keeler, D. A. Lockerby, S. Kumar, and J. E. Sprittles, Stability and bifurcation of dynamic contact lines in two dimensions, J. Fluid Mech. **945**, A34 (2022).

[11] D. Lohse, Fundamental fluid dynamics challenges in inkjet printing, Annu. Rev. Fluid Mech. **54**, 349 (2022).

[12] K. G. Winkels, I. R. Peters, F. Evangelista, M. Riepen, A. Daerr, L. Limat, and J. H. Snoeijer, Receding contact lines: From sliding drops to immersion lithography, Eur. Phys. J.: Spec. Top. **192**, 195 (2011).

[13] D. Bonn, J. Eggers, J. Indekeu, J. Meunier, and E. Rolley, Wetting and spreading, Rev. Mod. Phys. **81**, 739 (2009).

[14] H. A. Stone, A. D. Stroock, and A. Ajdari, Engineering flows in small devices: Microfluidics toward a lab-on-a-chip, Annu. Rev. Fluid Mech. **36**, 381 (2004).

[15] I. Cohen and S. R. Nagel, Scaling at the selective withdrawal transition through a tube suspended above the fluid surface, Phys. Rev. Lett. **88**, 074501 (2002).

[16] L. Limat and H. A. Stone, Three-dimensional lubrication model of a contact line corner singularity, Europhys. Lett. **65**, 365 (2004).

[17] J. H. Snoeijer, E. Rio, N. Le Grand, and L. Limat, Self-similar flow and contact line geometry at the rear of cornered drops, Phys. Fluids **17**, 072101 (2005).

[18] E. Ramé, K. Stoev, and S. Garoff, Effects of inertia on the hydrodynamics near moving contact lines, Phys. Fluids **11**, 3209 (1999).

[19] R. G. Cox, Inertial and viscous effects on dynamic contact angles, J. Fluid Mech. **357**, 249 (1998).

[20] T. S. Chan, Dynamical wetting transitions: Liquid film deposition and air entrainment, Ph.D. thesis, University of Twente, Netherlands, 2012.

[21] A. Varma, A. Roy, and B. A. Puthenveettil, Inertial effects on the flow near a moving contact line, J. Fluid Mech. **924**, A36 (2021).

[22] A. de Ryck and D. Quéré, Gravity and inertia effects in plate coating, J. Colloid Interface Sci. **203**, 278 (1998).

[23] A. Koulago, V. Shkadov, D. Quéré, and A. de Ryck, Film entrained by a fiber quickly drawn out of a liquid bath, Phys. Fluids **7**, 1221 (1995).

[24] H. Kim, C. Poelma, G. Ooms, and J. Westerweel, Experimental and theoretical study of dewetting corner flow, J. Fluid Mech. **762**, 393 (2015).

[25] H. Schlichting and K. Gersten, *Boundary-Layer Theory* (Springer-Verlag, Berlin, Heidelberg, 2000).

[26] D. Lo Jacono, F. Plouraboué, and A. Bergeon, Weak-inertial flow between two rough surfaces, Phys. Fluids **17**, 063602 (2005).

[27] E. J. Hinch, *Perturbation Methods*, Cambridge Texts in Applied Mathematics (Cambridge University Press, Cambridge, UK, 1991).

[28] R. G. Cox, The dynamics of the spreading of liquids on a solid surface. part 1. viscous flow, J. Fluid Mech. **168**, 169 (1986).

[29] J. H. Snoeijer, I. Peters, L. Limat, and A. Daerr, Simple views on cornered contact lines near instability, in *Proceedings of the 23rd Canadian Congress of Applied Mechanics* (Vancouver, Canada, 2011).

[30] J. H. Snoeijer, N. Le Grand-Piteira, L. Limat, H. A. Stone, and J. Eggers, Cornered drops and rivulets, Phys. Fluids **19**, 042104 (2007).

[31] I. Peters, J. H. Snoeijer, A. Daerr, and L. Limat, Coexistence of two singularities in dewetting flows: Regularizing the corner tip, Phys. Rev. Lett. **103**, 114501 (2009).